Kam et al. eLight (2026) 6:13
https://doi.org/10.1186/s43593-026-00124-1
elight.springeropen.com

RESEARCH ARTICLE Open Access

Quantum skyrmions and high dimensional entanglement mediated by nanophotonics

Amit Kam[1,2], Shai Tsesses[3,4], Lior Fridman[2,3], Yigal Ilin[2,3], Amir Sivan[2,3], Guy Sayer[2,3], Stav Lotan[2,3], Kobi Cohen[3,5], Amit Shaham[3], Liat Nemirovsky-Levy[1,2,5], Larisa Popilevsky[6], Aviv Karnieli[2,3], Meir Orenstein[2,3,6], Mordechai Segev[1,2,3,5] and Guy Bartal[2,3,6*]

Abstract

Quantum nanophotonics offers essential tools and technologies for controlling quantum states, while maintaining a miniature form factor and high scalability. Nanophotonic platforms can transfer information from the traditional degrees of freedom (DoFs) of photons, such as spin angular momentum (SAM) and orbital angular momentum (OAM), to the DoFs of the nanophotonic platform—and back, opening new directions for quantum information processing. Recent experiments have utilized, for entanglement the total angular momentum (TAM) of a photon—as a unique DoF of nanophotonic platforms—for demonstrating entanglement in TAM. Here, we unravel the morphing of quantum states of heralded single photons as they couple into and out of the near-field of a nanophotonic system. Through quantum state tomography, we discover that the TAM state of the near-field transforms to a free-space entangled state within a larger Hilbert space of SAM and OAM. Furthermore, we show that this entangled single photon state is in fact a quantum optical Stokes skyrmion with a topological invariant of ±2. The concepts described here bring new ideas and methodologies in developing high-dimensional quantum circuitry on a chip.

Keywords Nanophotonics, Quantum optics, Quantum skyrmions, Quantum state tomography, Near-field, High-dimensional entanglement, Total-angular momentum

1 Introduction

Quantum optics at the nanoscale explores the enhanced interaction between photons and emitters at the sub-wavelength level [1, 2], as well as the possibilities to engineer the optical environment of photons via nano-structuring, to produce new quantum states of light [3–5]. Applications of quantum nanophotonics range from quantum communications [6–8] and sensing [9, 10] to computation [11–13] within compact dimensions and in a scalable chip-based platform [14, 15]. In this vein, photons are versatile carriers of quantum information, capable of encoding qubits across a variety of degrees-of-freedom (DoFs), including propagation direction [16], time [17] or frequency-bin [18], spatial mode shape [19–23] and polarization [24–26]. The latter two DoFs are both related to angular momentum: an angular phase gradient is related to orbital angular momentum (OAM), while circular polarization manifests the spin angular momentum (SAM) of a photon [27–29]. Under the paraxial approximation, where the shape of the photonic wavepacket varies slowly on the wavelength scale, these DoFs are separable. This allows for more quantum

*Correspondence:
Guy Bartal
guy@ee.technion.ac.il
[1] Physics Department, Technion – Israel Institute of Technology, 32000 Haifa, Israel
[2] Helen Diller Quantum Center, Technion – Israel Institute of Technology, 32000 Haifa, Israel
[3] Andrew and Erna Viterbi Department of Electrical and Computer Engineering, Technion – Israel Institute of Technology, 32000 Haifa, Israel
[4] Department of Physics, MIT-Harvard Center for Ultracold Atoms and Research Laboratory of Electronics, Massachusetts Institute of Technology, Cambridge, MA 02139, USA
[5] Solid State Institute, Technion – Israel Institute of Technology, 32000 Haifa, Israel
[6] Russell Berrie Nanotechnology Institute, Technion, 32000 Haifa, Israel

information to be encoded on individual photons, either directly on their angular momentum [30–32], or through topological texture in synthetic space such as Stokes skyrmions [33, 34], with improved robustness [35–37]. However, when photons are tightly confined on the scale of their wavelength, the SAM and OAM become inseparable [38, 39]. This results in diverse classical and quantum consequences, ranging from formation of novel nanophotonic field textures, such as optical field-skyrmions [40, 41], to the creation of new quantum states related to total angular momentum (TAM) [42–45]. Recent work has highlighted the significance of these findings for quantum information science, specifically by entangling nanophotonic states on their TAM basis [46].

Here, we show that the TAM nanophotonic quantum states generated in our system are projected onto entangled complex states in a larger Hilbert space consisting of four orthogonal modes when coupled out to free-space, which can be exploited as qudits through selective measurements. Using Quantum State Tomography (QST), we reveal that the near-field photon carrying TAM displays a unique transverse two-dimensional vectorial texture [47, 48]. We find that our nanophotonic system naturally generates a single-photon entangled Stokes skyrmion [49–55] directly from the TAM states, when coupled out to free space. We map this skyrmion using heralded single photons, extract its topological number, and show that this skyrmion exhibits entanglement between its SAM and OAM.

This study highlights the unique evolution of the quantum information held by photons as they propagate through a nanophotonic platform, demonstrating the generation of quantum skyrmions directly from the TAM states. This paves the way for novel on-chip source for qudits with judiciously engineered properties towards scalable, high-dimensional quantum information processing and architectures that exploit topological invariants as a robust quantum degree of freedom.

2 Results

We employ a surface plasmon platform (Fig. 1a) consisting of a gold-air interface patterned with a circular grating, specifically designed for coupling light into surface plasmon polariton (SPP) modes $|J_n\rangle$ carrying angular momentum [38, 56–59]. In such systems, the TAM of a photon, $j = n\hbar$ cannot be separated into independent contributions of proper SAM and OAM. Instead, the angular momentum of any near-field state is characterized only by the TAM it carries. This vectorial modal field can be expressed in terms of its

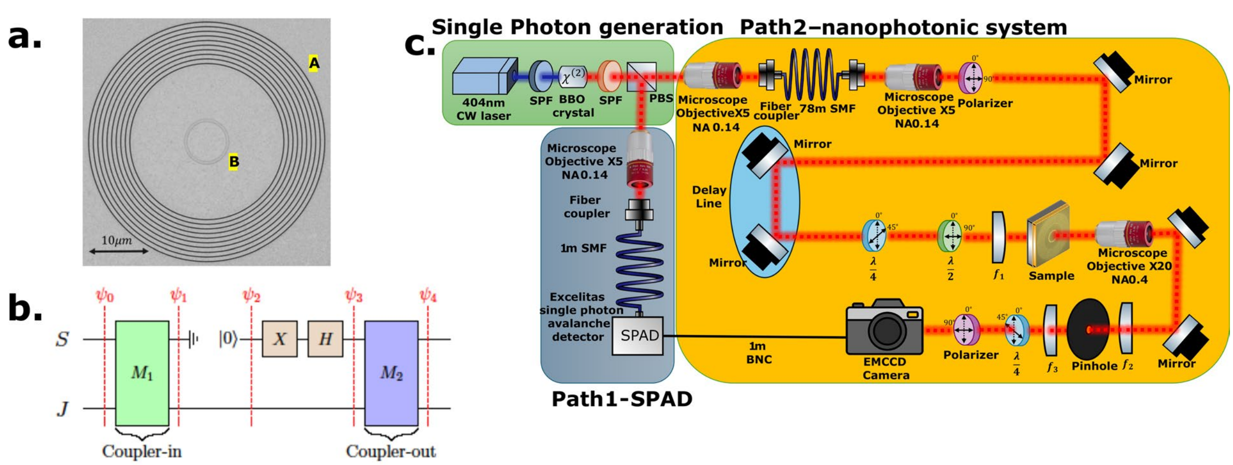

Fig. 1 Experimental apparatus for heralded detection of entanglement in nanophotonic modes: **a** SEM micrograph of the nanophotonic system—a nanopatterned gold layer evaporated on a glass substrate. The circular input coupler (**A**), which couples photons of a given polarization to plasmons with a well-defined TAM, is milled through the entire gold layer. The annular out-coupler ring (**B**) is milled only through half of it, scattering the SPPs into photonic modes propagating towards the camera. **b** Schematic representation of the nanophotonic platform as a quantum circuit utilizing two DoFs of the launched photon. (See supplementary for the derivation as a quantum channel). **c** Experimental setup: a 404 nm CW laser beam is directed into a BBO type- II crystal to produce photon pairs via spontaneous parametric down conversion (SPDC). The photon pairs are filtered to allow only collinear, same-frequency photons at 808 nm, distinguishable only by their orthogonal linear polarizations. The photons are separated into two different paths using a polarizing beam splitter (PBS). The first (heralding) photon is coupled into a single-mode fiber and sent to a single-photon detector, whose signal triggers the EMCCD camera and ensures it only detects coincident single photon events. The second photon is coupled into a different single-mode fiber, then enters a delay line to synchronize the timing between the heralding signal and the photon arrival on the EMCCD camera. After passing through waveplates to control its polarization, the photon is incident upon the nanophotonic system (denoted as 'sample'). Once scattered, the outgoing photon passes through waveplates to project the quantum state onto different polarization components

cartesian unit vector components (X, Y, Z), or by in-plane rotating field components ($\mathrm{LH} = \frac{X+iY}{\sqrt{2}}$, $\mathrm{RH} = \frac{X-iY}{\sqrt{2}}$, Z) with their respective spatial distribution. In particular, the LH, RH components of a nanophotonic mode generated by an incident circularly-polarized photon can be described by Bessel-type modes, while a linearly polarized input transforms into a superposition of such Bessel modes and can be represented by Hermite-Bessel-type modes [60–63]. Thus, the polarization of a photon coupled into our nanophotonic systems determines which nanophotonic modes are excited (Bessel or Hermite-Bessel type). These nanophotonic modes are subsequently coupled out to free-space via a concentric annular slit carved half-way into the gold layer. As we recently showed [46], the circular symmetry of this system preserves the angular momentum properties in the out-coupling process, facilitating the study of angular momentum transfer in nanoscale photonic systems.

In general, SPPs generated in such circularly-symmetric nanophotonic platform are either eigenstates of the TAM operator with a TAM value equal to that of the incident free-space photon, or their coherent superpositions [46]. The TAM eigenstates correspond to the n^{th} order transverse magnetic (TM) Bessel mode $|J_n\rangle$ carrying $j = n\hbar$ angular momentum. Note that mapping an incident photon to a near-field mode is not a reciprocal transformation—since only the TAM is conserved in the coupling, e.g., both free-space photonic states $|\sigma_+\rangle \otimes |l = 0\rangle$ and $|\sigma_-\rangle \otimes |l = 2\rangle$ will excite the same SPP mode with TAM of $j = 1\hbar$. The value $\sigma\hbar$ is the SAM of the input photon for left-handed ($\sigma = -1$) or right-handed ($\sigma = +1$) circularly polarized mode and $l = n\hbar$ (for integer n) are the OAM eigenvalues manifested by an azimuthal phase of $\exp(in\phi)$ of the electromagnetic field. In our case, we generate such SPP states by launching into the nanophotonic system paraxial photons carrying only SAM.

The incident photons are transformed into SPP modes with a well-defined TAM (or their superposition) per photon, which is equal to the SAM of the incident photon. Specifically, $|\sigma_-\rangle$ ($|\sigma_+\rangle$) circular polarization generates a nanophotonic state of $|J_{-1}\rangle$($|J_{+1}\rangle$). Namely, the z-component of the nanophotonic mode is shaped radially as a Bessel function of the first kind of order $-1\,(+1)$ carrying a $-\hbar$ $(+\hbar)$ quantum of angular momentum. Likewise, the linear polarization states $|H\rangle$, $|V\rangle$,which are superpositions of circular polarizations ($|H\rangle = \frac{|\sigma_+\rangle+|\sigma_-\rangle}{\sqrt{2}}$, $|V\rangle = \frac{|\sigma_+\rangle-|\sigma_-\rangle}{\sqrt{2}i}$), generate a superposition of SPP Bessel modes $|J_\pm\rangle = \frac{1}{\sqrt{2}}(|J_1\rangle \pm |J_{-1}\rangle)$. Equation (1) summarizes the excitation of these four possible nanophotonic modes as a function of polarization of the incident photon:

$$
\begin{aligned}
&|\sigma_+\rangle \otimes |l=0\rangle && \mapsto |J_{-1}\rangle \\
&|\sigma_-\rangle \otimes |l=0\rangle && \mapsto |J_{-1}\rangle \\
&|H\rangle \otimes |l=0\rangle = \frac{|\sigma_+\rangle + |\sigma_-\rangle}{\sqrt{2}} \otimes |l=0\rangle && \mapsto |J_+\rangle \\
&|V\rangle \otimes |l=0\rangle = \frac{|\sigma_+\rangle - |\sigma_-\rangle}{\sqrt{2}i} \otimes |l=0\rangle && \mapsto |J_-\rangle
\end{aligned}
\tag{1}
$$

where $\mapsto$ indicates the in-coupling operation. The ideal coupling of the input field into the nanophotonic mode facilitates the generation of a qubit encoded in the TAM basis.

The generated plasmons are scattered out by an annular coupler. The transversal nature of the out-scattered photon is equivalent to a radiation source which is generated from the in-plane components of the SPP field overlapping with the annular perturbation. Thus, not only the TAM value of the near-field is preserved in this scattering process but also the detailed in-plane vectorial pattern of the near-field mode. However, in the far-field of the annular coupler, the field emanated from the slit is paraxial, hence the angular momentum of the scattered field can be decomposed to its SAM and OAM constituents. This gives rise to a unique transformation of the TAM of the near-field photon, embedded in its in-plane vectorial spatial distribution $|J_n\rangle$, to SAM-OAM entanglement of the free-space photonic state:

$$
|J_n\rangle \mapsto \frac{1}{\sqrt{2}}\left(|\sigma_-\rangle|l = n+1\rangle - |\sigma_+\rangle|l = n-1\rangle\right) \tag{2}
$$

where $\mapsto$ represents here out-coupling operation and $n \in (-1,1)$ in our system. The state $|l = n \pm 1\rangle$ is defined as $|l = n \pm 1\rangle = \int_0^{2\pi}\int_0^{r_a} N_{n\pm1} j_n(kr) e^{i(n\pm1)\theta} r dr d\theta$, where r_a represents the mode radius determined experimentally where the photon detection probability decays to below noise level, and N_i is the normalization factor of the corresponding state. Note that for $n = 0$, the nanophotonic mode has full radial symmetry, lacking any azimuthal dependence, and thus the state transforms as: $|J_0\rangle \mapsto \frac{1}{\sqrt{2}}\left(|\sigma_+\rangle|l = -1\rangle - |\sigma_-\rangle|l = 1\rangle\right)$.

This entanglement is the unique result of the fact that the angular momentum of the vector SPP mode is solely characterized by the observable TAM, and that only two combinations of SAM and OAM can preserve the TAM when light is coupled out to the far-field and there is no preferred combination due to the circular symmetry of the out-coupler. Thus, the out-coupled photon is in a superposition state of all combinations of the given TAM, where each component of the superposition is an independent mode of the free space propagation. Considering

Eqs. (1) and (2) together, out-coupling from the nanophotonic platform yields the resulting states:

$$\begin{aligned} &|J_1\rangle && \mapsto \frac{1}{\sqrt{2}}(|\sigma_-\rangle|l=2\rangle - |\sigma_+\rangle|l=0\rangle) \\ &|J_{-1}\rangle && \mapsto \frac{1}{\sqrt{2}}(|\sigma_-\rangle|l=0\rangle - |\sigma_+\rangle|l=-2\rangle) \\ &|J_+\rangle = \frac{1}{\sqrt{2}}(|J_1\rangle + |J_{-1}\rangle) && \mapsto \frac{1}{\sqrt{2}}(|H\rangle|HB_{20}\rangle - |V\rangle|HB_{11}\rangle) \\ &|J_-\rangle = \frac{1}{\sqrt{2}}(|J_1\rangle - |J_{-1}\rangle) && \mapsto \frac{1}{\sqrt{2}}(|H\rangle|HB_{11}\rangle - |V\rangle|HB_{02}\rangle) \end{aligned} \tag{3}$$

where $|HB_{11}\rangle = i\frac{|l=-2\rangle-|l=2\rangle}{\sqrt{2}}$, $|HB_{20}\rangle = \frac{|l=2\rangle+2|l=0\rangle+|l=-2\rangle}{2}$ and $|HB_{02}\rangle = \frac{-|l=2\rangle+2|l=0\rangle-|l=-2\rangle}{2}$ are Hermite-Bessel free space modes. Evidently, starting with a single incident circularly-polarized photon will result in a scattered single far-field photon displaying entanglement between two modes with orthogonal SAM and OAM. The quantum structure borne on the scattered photon is composed of the four orthogonal states: $|\sigma_+\rangle|l=0\rangle = |1\rangle, |\sigma_-\rangle|l=0\rangle = |2\rangle, |\sigma_+\rangle|l=-2\rangle = |3\rangle, |\sigma_-\rangle|l=2\rangle = |4\rangle$. Similarly, launching a single linearly polarized photon results in a far-field photon displaying entanglement between two states composed of linear polarizations and their associated Hermite–Bessel modes. These states are again four orthogonal states:

$$|H\rangle|HB_{20}\rangle = |\tilde{1}\rangle, |V\rangle|HB_{11}\rangle = |\tilde{2}\rangle, |H\rangle|HB_{11}\rangle = |\tilde{3}\rangle, |V\rangle|HB_{02}\rangle = |\tilde{4}\rangle$$

Equations (1–3) map the evolution of the Hilbert-space dimensionality evolution from the free-space domain, through the nanophotonic platform, and back to free space. For the free space incident photon, before coupling to our nanophotonic structure, the photon is described only by its polarization, e.g., for circular polarization, the state of the incident photon is $|\sigma_+\rangle|\sigma_-\rangle$, with $|l=0\rangle$. This defines a two-dimensional single-photon subspace. In the nanophotonic regime (Eq. 1), each of the photons with SAM of $|\sigma_+\rangle$ or $|\sigma_-\rangle$, is coupled to a single near-field mode with TAM $|J_1\rangle$ and $|J_{-1}\rangle$ respectively, thus the dimensionality remains 2. The transverse near-field (Eq. 2) can be written $|\mathrm{LH}, l=0+\mathrm{RH}, l=2\rangle$ for $|\sigma_+\rangle$ input and $|\mathrm{LH}, l=-2+\mathrm{RH}, l=0\rangle$ for $|\sigma_-\rangle$ input. This may seem that already here we have 4 orthogonal states and as if entanglement is already established in the near field. But this is not the case and each of these two seemingly combination states is a vectorial field of a single mode of the near field and is not separable to sum of two modes.

The entanglement is established in the out-coupling process. Namely, upon out-coupling into free space by a circular centrosymmetric slit (Eq. 3), the internal field is transformed into free propagating photons while preserving the in-plane vectorial nature as well as the azimuthal phase gradient. Thus, each of the near-field modes is transformed into a state with similar transverse field pattern in free space. However, in free space each combination is actually of two self-modes of propagation (see Eq. (3)) and the dimensionality is increased to four and the combination state is an entangled state, as the entanglement is generated by the output coupler (similar to a beam splitter).

It is possible to model our nanophotonic system as a non-unital quantum channel represented by a non-unitary quantum circuit, as shown in Fig. 1b. The circuit acts on a composite system of two qubits, utilizing TAM and SAM degrees of freedom of the photon. The output of the quantum circuit in Fig. 1c is an entangled state between different combinations of the photon polarization and spatial distribution, with the input and output couplers, $\widehat{M}_1$ and $\widehat{M}_2$, acting as two-qubit unitary gates, while $\widehat{X}$ and $\widehat{H}$ represent the Pauli $\widehat{X}$ and Hadamard operators, respectively. The reduction in degrees of freedom in the near-field is modeled as a dissipative operation, where the action on a single-qubit state $|\psi\rangle$ is represented as $|\psi\rangle \rightarrow |0\rangle$. Consequently, the quantum system is both dissipative and entangling. Such dissipative and entangling circuits have recently been shown to enable methods for preparing a wide range of ground states, facilitating the representation of nontrivial thermal states with significantly enhanced noise resilience [64, 65], and able to eliminate the barren plateau effect in the training of quantum neural networks [66].

To fully utilize the extended high-dimensional Hilbert space of the emitted states, the evolution of the quantum states in the system needs to be thoroughly analyzed and understood. Typically, such a feat is accomplished through Quantum State Tomography (QST) [67, 68], which is being used to characterize many different quantum systems [69, 70], in particular the quantum states of light [71, 72]. QST determines the quantum state of a system by measuring various non-commuting observables on an ensemble of identically-prepared system copies, enabling the extraction of the density matrix. We perform quantum state tomography of the photonic state generated by passing through our entire apparatus (Fig. 1c). We use heralded detection, separating two photons generated via spontaneous parametric down-conversion in a nonlinear crystal and using one of them to trigger an Electron-Multiplying CCD (EMCCD) camera. Hence, the camera only captures heralded single photons scattered from the nanophotonic platform. The imaging system is set in the Fourier plane of the platform output coupler, recording the far field distribution of the detection probability of the modes. We make sure that, in a single acquisition frame, only one pixel is turned on by a single photon on average, and the camera records its position in the image plane of the structure output. We launch single photons into the platform at four different polarizations ($|H\rangle, |V\rangle, |\sigma_-\rangle, |\sigma_+\rangle$) using a quarter- (QWP) and half-wave plate (HWP) and use an additional set of waveplates and a polarizer to project the quantum state of the out-coupled photon onto these four polarization components, resolving their distribution via the camera.

Figure 2a presents the tomography measurement results for each polarization state of the incident photon. Using a Mean Squared Error (MSE) estimator, we fit each measurement result to a superposition of ideal Bessel or Hermite-Bessel modes (Fig. 2b), and infer that they all show excellent agreement with Eq. 1 and 3. Using the same MSE algorithm, we are able to reconstruct the density matrix for each of the 4 possibilities of the incident photon state (Fig. 3). We fit each spatial distribution obtained from the tomography to the spatial modes, determining the maximum likelihood coefficients.

Note that, while the TAM states in the nanophotonic platform are 2-dimensional, spanned by ($J_{\pm1}$), upon out-coupling to free space the photons attain a larger basis as the separate SAM and OAM become good observables again. This resides in Hilbert space of $2 \times 3 = 6$ dimensions (2 polarization $\times$ 3 spatial distribution, out of which, two modes are not populated in our specific experiment: $|\sigma_-\rangle|l = -2\rangle$ and $|\sigma_+\rangle|l = 2\rangle$ in one base, and $|H\rangle|HB_{02}\rangle$ and $|V\rangle|HB_{20}\rangle$) in the other.

The states in (Fig. 3) have the structure of a Bell state, i.e., they are naturally represented by 4×4 density matrix (describing the 2 populated states out of the 6 possible states total). But, when the same physical state is spanned in the alternative basis, it is more naturally described by a 6×6 density matrix (describing the 4 populated states out of the 6 possible states). The mapping between the bases is formally expressed as $\rho_{base2} = U\rho_{base1}U^{\dagger}$, where U is the unitary transformation. The transformation between the different free-space bases does not add information to the photon; rather, it reveals and resolves the underlying high-dimensional structure by expressing the state in a basis that includes all accessible polarization–spatial modes (see Supplementary Information for a detailed derivation).This enables us to analyze and visualize the same quantum state in a basis that is more suitable for revealing its higher-dimensional structure. An illustration of this mapping for two input photon states is presented in Fig. 4.

To gain deeper insight into the correlations between the spatial wavefunction of a photon and its polarization (specifically its SAM and OAM), we calculate the Wigner distribution of the photonic mode. This distribution represents the correlation between the in-plane vector field components. The Wigner distribution encodes quantum expectation values in phase-space (continuous variables), providing a concise representation of the quantum information in the system (see Supplementary for the derivation). For each input polarization, the two entangled output modes, denoted as α and β, have a real and imaginary parts, making it a 4D Wigner distribution corresponding to four

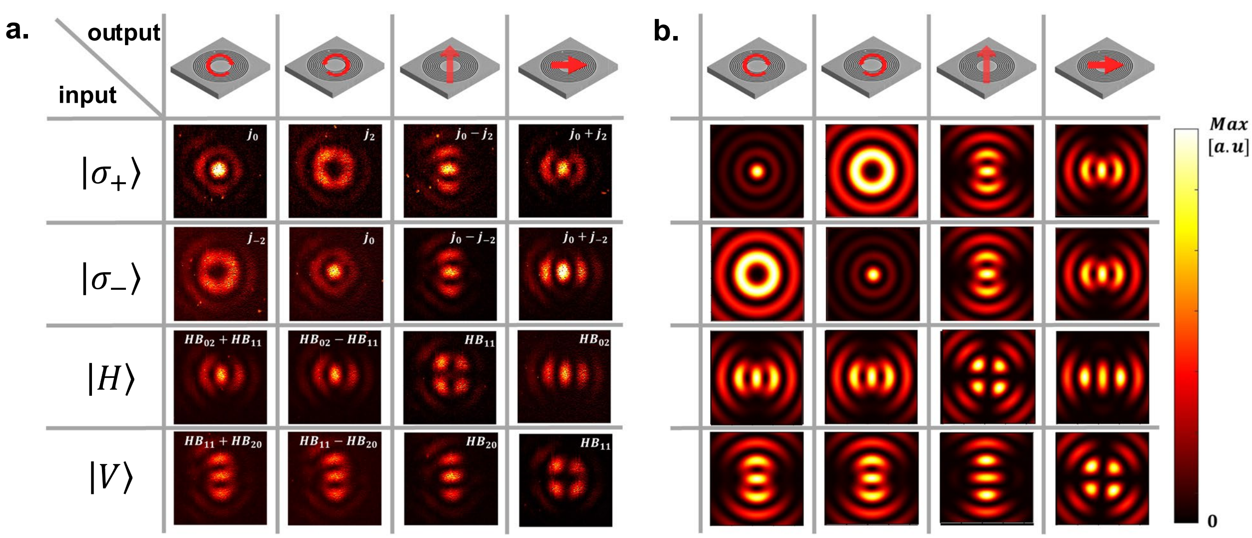

Fig. 2 Quantum state tomography of photonic free-space photons created from near-field qubits. The panels show the intensity of the projection of a heralded single photon on the four different polarizations, as recorded by an EMCCD camera. This action is performed for four different polarizations of the incident photon. The left column lists the 4 possibilities of the polarization of photons incident upon the nanophotonic system, while the top row lists the measured polarization. $|\sigma_\pm\rangle$: left – and right – circular polarizations (replicated from [46]). $|H\rangle$ and $|V\rangle$: horizontal- and vertical- linear polarizations. **a** Experimental results. **b** Fitting results (via mean squared error) for each intensity image to the state of the photon projected to ideal Bessel and Bessel-Hermite bases

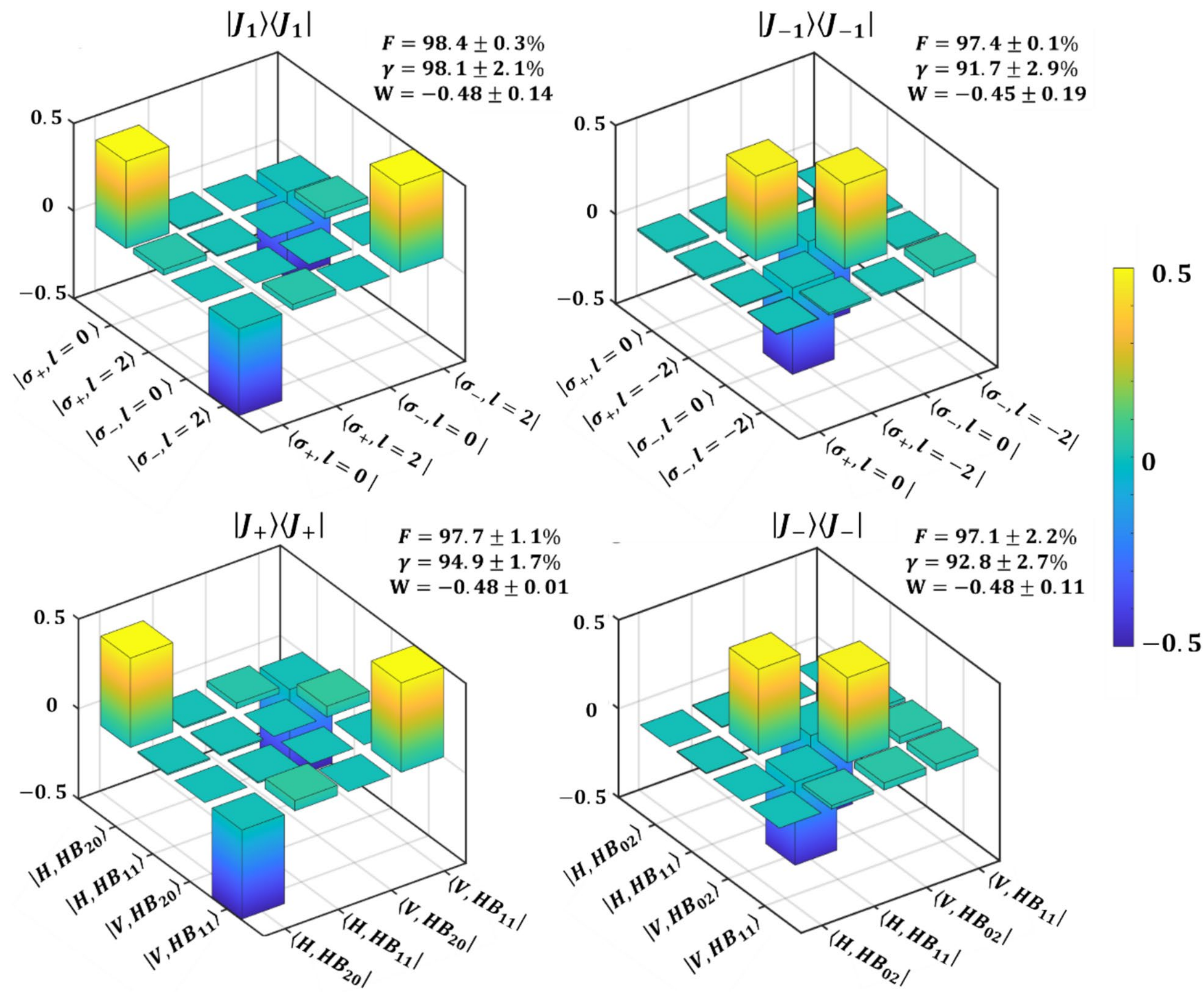

Fig. 3 Density matrices of the four Bell states. Experimentally measured density matrices recovered for each TAM state by the QST. The experimental results coincide with theoretical results with higher than 97% fidelity and 91% purity. The results shown here are the real parts only because the imaginary part is identically zero both theoretically and experimentally

phase-space coordinates. We plot the projections of the Wigner distribution onto six pairs of space-phase coordinates, with the two other coordinates at the origin (Fig. 5).

The two projections on the left-hand side of Fig. 5a represent the phase-space (real and imaginary) of each single mode $\Re(\alpha), \Im(\alpha)$ and $\Re(\beta), \Im(\beta)$ with a single excitation. The panels display negative values that attest to the non-classical nature of the state and a single ring as expected of a Wigner distribution for the Fock state $|1\rangle$. The two projections on the right-hand side of Fig. 5a do not exhibit correlations both between $\Re(\alpha), \Im(\beta)$ and $\Re(\beta), \Im(\alpha)$ phase-space cross-mode coordinate pairs, since they can be decomposed into a sum of products of the single-mode Wigner distributions corresponding to the Fock states $|0\rangle$ and $|1\rangle$, see Supplementary. However, entanglement between the two modes is clearly evident in the two projections in the middle column, which exhibit nonclassical correlations between the pairs of phase-space coordinates $\Re(\alpha), \Re(\beta)$ and $\Im(\alpha), \Im(\beta)$ belonging to different modes. This can be surmised visually from the fact that the related Wigner distribution is not symmetric about its two axes and thus cannot be the outer product of two symmetric 1D quasiprobability functions along phase-space coordinates corresponding to Fock number states 0 and 1 in the two modes, as explained in the Supplementary. Our measured results agree with the

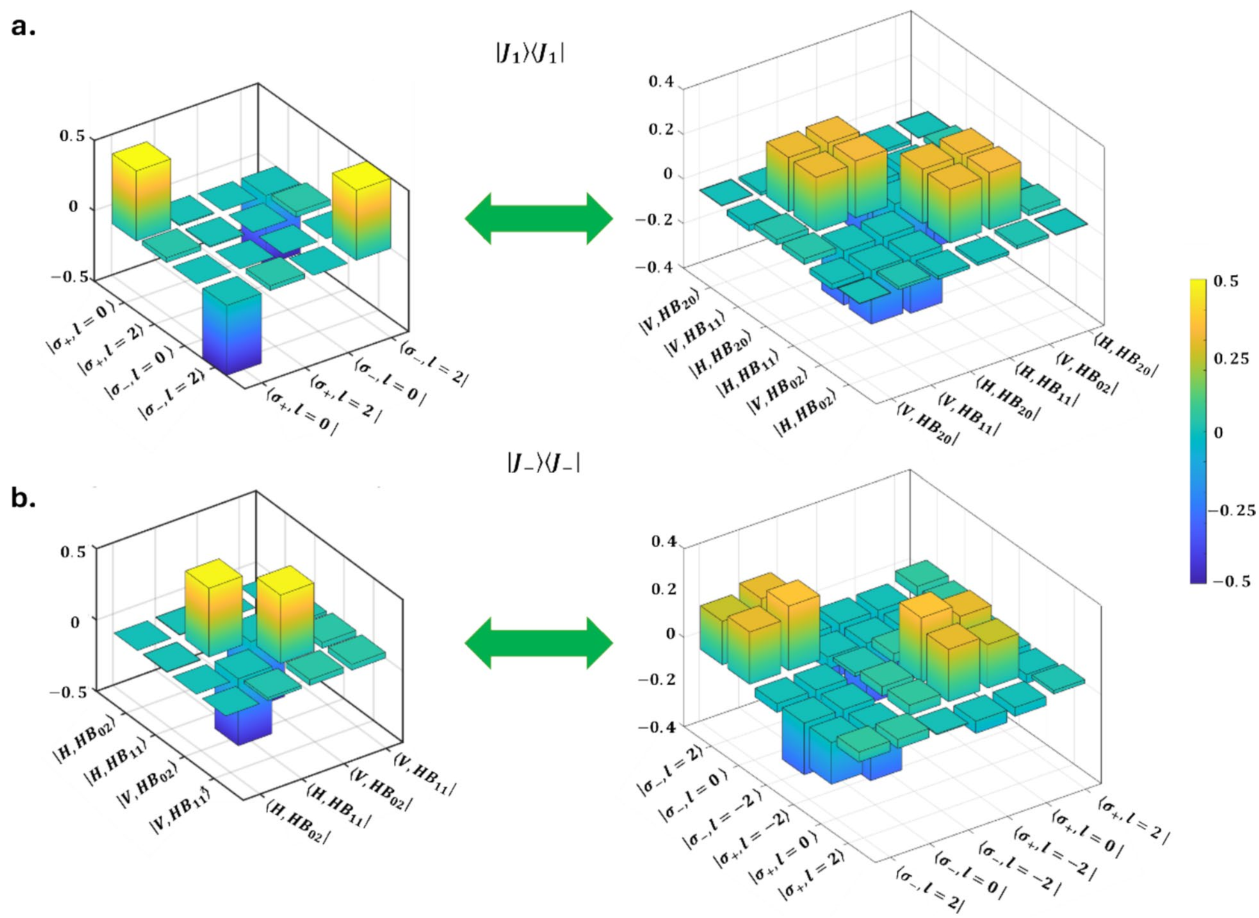

Fig. 4 Transformation between free-space qudit density matrices. **a** The 4X4 density matrix orienting from the TAM eigenstate J_1 transformed into a 6X6 density matrix in the linear-polarization and HB modes Hilbert space. **b** The 4X4 density matrix orienting from the TAM superposition state J_{-}, transformed into a 6X6 density matrix circular-polarization and Bessel-modes Hilbert space

theoretical Wigner distribution to an excellent degree, as seen from the differences between the theoretical and measured 2D projections of the Wigner distributions, shown in Fig. 5b.

Interestingly, the event of a single circularly polarized photon coupled into the nanophotonic platform results in an out-coupled free-space photon with a unique structure: *a Stokes skyrmion displaying entanglement properties.* Calculating the Stokes vector $\mathbf{S}(x, y, z)$ of the output photon field affirms that the topological structure forms a quantum Stokes Skyrmion, whose topological number is $N = \frac{1}{4\pi}\iint \boldsymbol{S}\cdot\left(\frac{\partial \boldsymbol{S}}{\partial x}\times\frac{\partial \boldsymbol{S}}{\partial y}\right)dxdy \approx -2(2)$ for right (left) circular polarized input photon, where $\boldsymbol{S}(\mathrm{x,y,z}) = \frac{(S_1,S_2,S_3)}{S_0}$ represents the 3D normalized Stokes vector $(S_0 = |E_H|^2 + |E_V|^2, S_1 = |E_H|^2 - |E_V|^2, S_2 = |E_A|^2 - |E_D|^2, S_3 = \left|E_{\sigma_+}\right|^2 - \left|E_{\sigma_-}\right|^2)$. The pertinent components are obtained from our polarization-resolved single-photon measurements in the linear $(|H\rangle, |V\rangle)$, diagonal $(|A\rangle, |D\rangle)$, and circular $(|\sigma_+\rangle, |\sigma_-\rangle)$ polarization bases. See Supplementary for detailed explanation about skyrmion generation using a circular slit.

Figure 6 shows the measured Stokes-field distribution obtained from our measurements for a heralded input right circularly polarized photon that initially carries TAM of $+1\hbar$. From the experimental data, we extract $N_{\mathrm{exp}} = -1.911 \pm 0.236$ which is in excellent agreement with the designed value of $N = -2$.

The robustness of our skyrmion formation is primarily a consequence of how the skyrmion is generated: the skyrmion texture is encoded and locked within the TAM eigenstate of the SPP mode, hence the skyrmion is generated intrinsically by the device, without any need to be synthesized by aligning and phase-locking multiple free-space beams. This strongly reduces the vulnerability to delicate relative phase drifts and beam-pointing instabilities that typically limit dual-beam or interferometric skyrmion schemes. Furthermore, the generated skyrmion is not hoovering between different skyrmion types in propagation since the propagation constant of

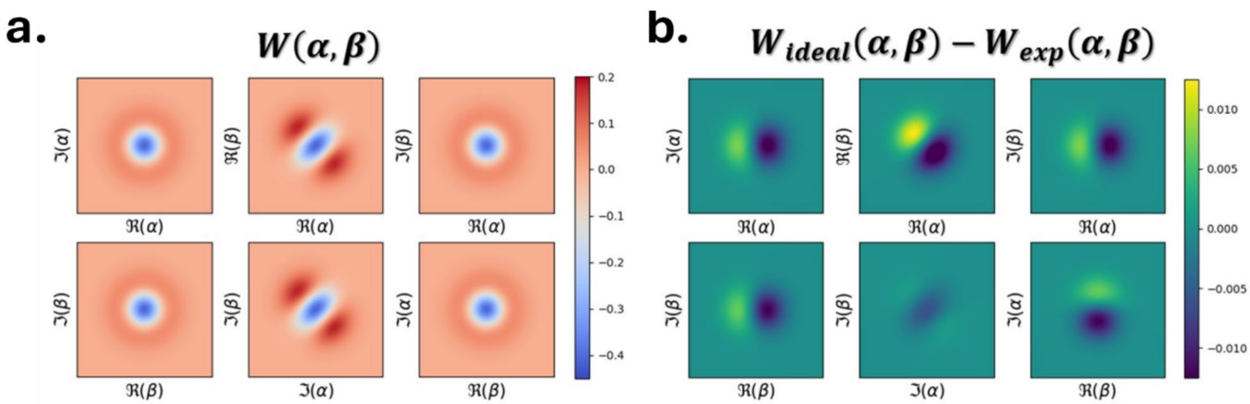

Fig. 5 Wigner function of the photon derived from the nanophotonic mode. The figure displays six slices of the four-dimensional Wigner function of the modes (α, β), each representing a projection onto two components of the two modes. Non-classicality is readily identified by negative values (blue in Fig. 5) of the quasiprobability distribution, whereas entanglement is manifested as interference between modes. For a non-separable two-mode state, the joint Wigner function in the cross coordinates $\Re(\alpha)\Re(\beta)$ and $\Im(\alpha)\Im(\beta)$ cannot be written as a sum products of two single-mode quasiprobabilities. This inseparability appears as a diagonally distributed pattern that cannot be decomposed into a sum of independent Wigner functions. **a** Example of the Wigner function for the state $|J_1\rangle$. **b** Difference between the ideal Wigner function and the experimentally computed one. The various images reveal an asymmetry on the order of 10^{-2}, which could be attributed to the partial presence of the $|J_{-1}\rangle$ state in the system's basis, The small deviations do not alter the overall state fidelity, which remains consistent with the value obtained from the reconstructed density matrix

both its constituents is equal and thus the relative phase is preserved.

3 Discussions and conclusions

In conclusion, we generated entangled single-photon states, encoded in the polarization and spatial-mode degrees of freedom, using a nanophotonic platform. These entangled states utilize the vector nature of TAM modes created in the near-field and the unique way they are coupled into free-space. We employed QST to analyze the quantum information imprinted on the emitted photons and found that the nanophotonic system creates higher dimensional entangled photon states which could be used as qudits. The non-trivial topology of the output single photons from our nanophotonic platform was robustly mapped into a free-space to form Stokes skyrmion without post-selecting the skyrmionic component from a more complex quantum state [33, 34]. Furthermore, in our experiments, this single-photon entangled skyrmion is naturally generated by the nanophotonic platform and does not require dual-beam implementations to synthesize the vector field [73] nor multi-photon entanglement [35]. Such quantum skyrmions are predicted to remain robust even under strongly perturbing channels [35, 37, 74, 75], making them promising candidates for realistic, high-dimensional quantum links.

While high-dimensional states have been previously realized in various platforms, this higher dimensional single-photon states are uniquely initiated by TAM of the near-field mode. As such, it may lead to new sources of entangled states of light, such as quantum astigmatic states (achieved through judiciously shaped couplers) [76], fractional states (using spiral couplers with fractional helicity) [77] and hyper-entangled state [78], all of which exhibit a vector structured wavefunction in the near-field with embedded entanglement between their DoFs in the far-field. Additionally, the nanophotonic platform can serve as a quantum multiplexer or demultiplexer for quantum communications, enabling the entanglement of multiple photon DoFs. Finally, our nanophotonic platform provides a possible route toward qudit-based QKD [79], relying on the same device geometry. Our platform is well-suited for integration with a wide range of on-chip photonic circuits and could be extended to achieve higher-order entanglement by coupling multiple photons to the nanophotonic system, advancing on-chip quantum technologies. Furthermore, it offers the potential for generating novel quantum states of light with SAM and OAM by leveraging nonlinear interactions between a strong free-space pump and quantum surface-confined states, as in references [80–82].

4 Methods

1.Sample fabrication

For sample fabrication Fig. 1a, we deposit a 220 nm gold layer upon a 1mm NBK7 glass substrate using e-Gun evaporation (Airco Temescal FC-1800, deposition rate:5 nm/sec) and mill the in- and out-couplers using a focused Ga ion beam (FEI Helios NanoLab

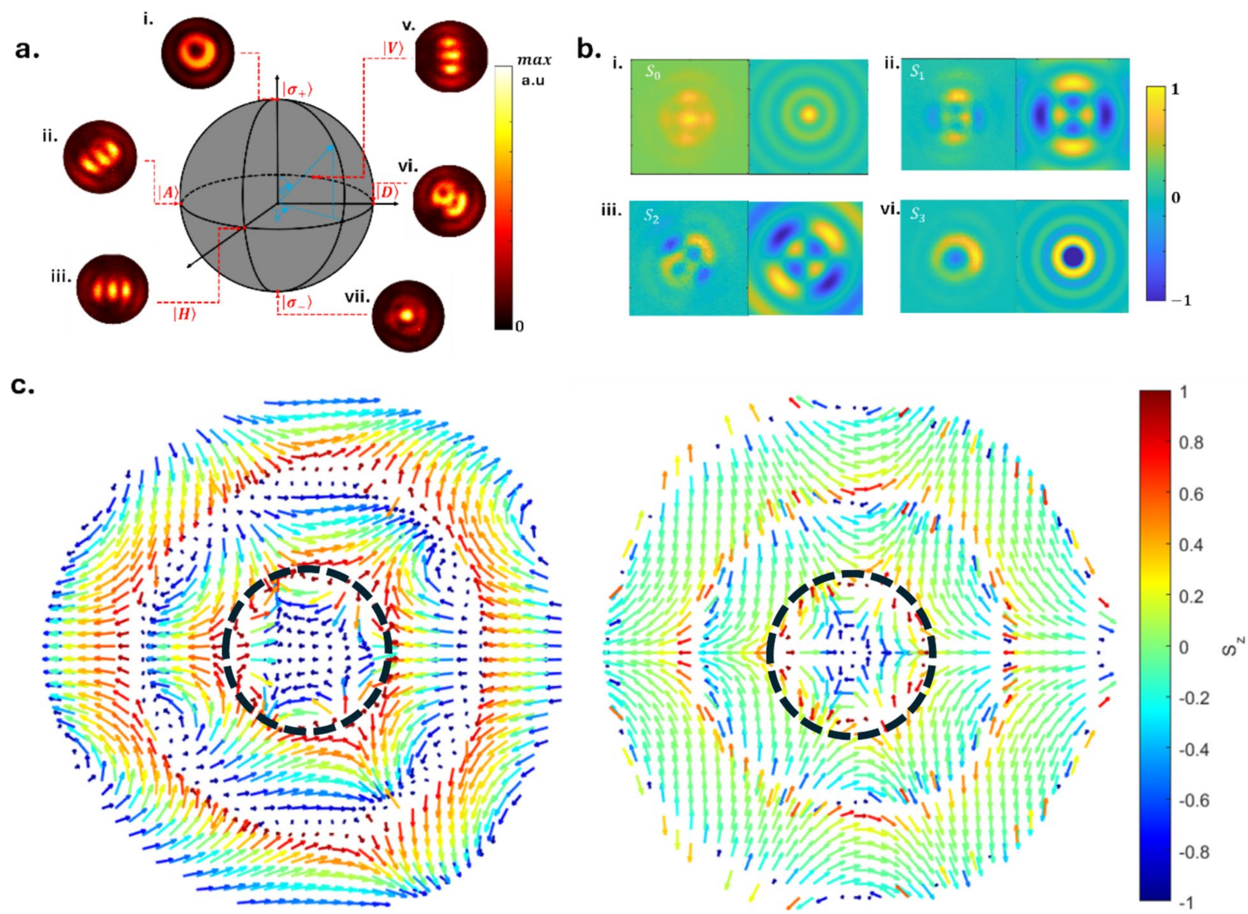

Fig. 6 Generation of the quantum photonic skyrmion. **a** Tomographic measurements at different points on the Poincaré sphere, representing a specific spatial mapping of polarization states. Linear polarization states are on the equator, circular polarization states are at the poles, and elliptical states are represented by points in between. **b** Reconstructed and calculated Stokes representation **c** Vector representation of the unit vector of the electric field (color coded for the value of its axial component red = 1and blue = −1), showing generation of anti-skyrmion with topological invariant of −2. Left: Reconstruction, and Right: Simulation. We obtain $N = -1.911 \pm 0.236$

DualBeam G3 UC, accelerating voltage: 22 keV, current: 7.7 pA, homemade software).

a.Coupling efficiency and sample dimension

In order to optimize the coupling efficiency of SPPs, we used the Fourier model method to estimate the coupling coefficient for various combinations of slit width and periodicity of the grating. The simulation shows that the coupling coefficient of the input coupler is calculated to be approximately 7% to 9% and the coupling coefficient of the out coupler is calculated to be approximately 10% to 15% for illumination at a wavelength of 808 nm. The total coupling coefficient for one photon in and out of the plasmonic system is approximately $7 \cdot 10^{-3}$ (this number agrees well with the average flux of scattered photons. The circular input coupler is milled through the entire gold layer with 10 grating periods, inner radius of $r_1 \approx 13.4\mu m$, outer radius of $r_2 \approx 20.9\mu m$ and grating line width of $\sim \frac{\lambda_{spp}}{4}$. The circular out-coupler is milled to a depth of 80 nm of the gold layer with inner radius of $r_1 \approx 5.39\mu m$ and outer radius of $r_2 \approx 5.97\mu m$, scattering only SPPs towards the camera.

b.In-plane SPP decay

The surface plasmon polariton propagates along the surface with a wave vector of k_{spp} as a surface wave: $k_{spp} = \frac{2\pi}{\lambda}\sqrt{\frac{\varepsilon_1\varepsilon_2}{\varepsilon_1+\varepsilon_2}} = \frac{2\pi}{0.808}\sqrt{\frac{-24.718+1.5517j}{1+-24.718+1.5517j}}$, where λ is the wavelength in vacuum and ε_1 and ε_2 are the permittivity of the two materials of the two sides of the interface. The propagation distance in this case is calculated by the inverse of the imaginary part of k_{spp}, as it introduces the decaying part of the field. Taking $\lambda = 808[nm]$,

$\varepsilon_1 = 1$ for air and $\varepsilon_2 = -24.718 + 1.5517j$ for gold at wavelength of 808 nm, we obtain $k_{spp} = 7.938 + 0.0105j\left[\frac{1}{\mu\mathrm{m}}\right]$. This calculation yields a propagation distance of $\frac{1}{0.0105} \approx 95.6[\mu\mathrm{m}]$. In addition, the exponential decay along the propagation between the input coupler to the output coupler (which was 7.6 μm long) can be calculated as well by the following: $e^{-\frac{7.6}{95.6}} = 0.9236$. Similarly, the decay of the SPP in the out coupler (which was 10.8 μm wide) is: $e^{-\frac{10.8}{95.6}} = 0.8932$. This means that the SPP field has lost approximately 8% of its amplitude by propagating from the input to the output coupler and 11% in the output coupler. Calculating for the standing wave ratio (SWR) of the field we obtain a SWR of: $SWR = \frac{1+0.8932}{1-0.8932} = 17.72$. This value indicates a dominantly standing wave in the output coupler region, that is accurately approximated to a spatial Bessel function.

c.Photons penetration depth

The wave vector of photons that propagate through a nonmagnetic medium is given by $k = \frac{2\pi}{\lambda}\sqrt{\varepsilon}$. By taking $\lambda = 808[\mathrm{nm}]$ and $\varepsilon = -24.718 + 1.5517j$ for gold at wavelength of 808[nm] we find that the wave vector of a 808 nm beam that propagate through gold is $k = 1.212 + 38.68j\left[\frac{1}{\mu\mathrm{m}}\right]$. Using the imaginary part of the wave vector, we find that the propagation distance of a 808 nm beam through the gold is approximately $\frac{1}{38.68}[\mu\mathrm{m}] \approx 25.9[\mathrm{nm}]$. This assures that the field we measure on the top side of the gold film is a result of the SPP field and not of the original signal, as it experiences a decay of over 6 times the propagation depth.

2.Experimental layout

Our experimental setup is described in Fig. 1.b of the main text. The photon pairs are produced via type-II SPDC using 5mm long a BBO crystal with 5X5mm cross section. (Newlight S/N: NCBB05500-404(II)). We use a pump laser of 404nm wavelength (Toptica iBEAM smart HP_14762) at 25.7°C to emit quasi-monochromatic light of ~ 300 mW power and beam diameter of 0.5 ± 0.1 mm. The crystal is aligned to produce two tangential cones. A $404 \pm 2nm$ filter is placed after the laser output to reduce any remaining light at the SPDC wavelength and unwanted amplified spontaneous emission. A 808 ± 1.5 nm band-pass filter is used to block pump photons after the crystal, together with two $810 \pm 10nm$ band-pass filters before the camera.

The photons are separated using polarizing beam splitter, where one photon is coupled into a single-mode fiber (P1-780Y-FC-1) by microscope objectives is an NIR APO X5, 0.14 NA towards a single mode detector (Excelitas SPCM-NIR) to trigger the EMCCD camera, synchronizing the detection of the photon from the nanophotonic platform which been delayed by 78m of single mode fiber. The camera is an EMCCD (Andor Ixon Ultra 888) operating at − 80 ℃, horizontal pixel shift readout rate of 30 MHz at 16-bit, vertical pixel shifts every 2.2 µs, and vertical clock amplitude voltage of 4V above the factory setting and at the maximal amplification gain, with an extended water-cooling system. The outgoing photon is also passed through waveplates to project the quantum state onto two different polarization components. The lenses in the setup have an effective focal length of 200 mm and the sample microscope objectives is an NIR APO X20, 0.4 NA (Mitutoyo S/N: 378-824-5).

Abbreviations

DoFs	Degrees of freedom
SAM	Spin angular momentum
OAM	Orbital angular momentum
TAM	Total angular momentum
QST	Quantum state tomography
SPP	Surface plasmon polariton
SPDC	Spontaneous parametric down conversion
PBS	Polarizing beam splitter
BBO	β-Barium borate
EMCCD	Electron-multiplying charge-coupled device
QWP	Quarter wave plate
HWP	Half wave plate
MSE	Means squared error
QKD	Quantum key distribution
NA	Numerical aperture
SWR	Standing wave ratio
SPAD	Single-photon avalanche diode

Supplementary Information

The online version contains supplementary material available at https://doi.org/10.1186/s43593-026-00124-1.

Supplementary Material 1.

Acknowledgements

This research was supported by the Israeli innovation authority trough the MAGNET program, Grant number 73756, and was supported by the Israel Science Foundation (ISF), Grant number 3620/24 and was funded by the German-Israel program known as DIP. We acknowledge the Russell Berrie Nanotechnology Institute, Micro-Nano Fabrication Unit (MNFU) and Hellen Diller Quantum Center for their support of this research. A.K. acknowledges the support from Azrieli fellowship, and the support from the Helen Diller Quantum Center at the Technion. S.T. acknowledges support from the Adams fellowship program of the Israel Academy of Science and Humanities, the Rothschild fellowship of the Yad Hanadiv foundation, the VATAT-Quantum fellowship of the Israel Council for Higher Education, the Helen Diller Quantum Center postdoctoral fellowship the Viterbi fellowship of the Technion – Israel Institute of Technology.

Author contributions

G.B., M.O, S.T. and M.S. conceived the project. A.K., L.F., L.P and K.C. designed and fabricated the samples. A.K., S.T. and L.F. build the experimental platform. A.K., L.F. and S.T. conducted the measurements. A.K., A.S., A.S., S.L, G.S. and Y.I. performed simulations and analyzed the experimental results. A.K., A.S., A.S., L.N.L., S.T, and M.O. conducted the theoretical calculations. G.B., M.O. and M.S. supervised the project. All authors participated in writing the manuscript.

Funding
MAGNET program, 73756, Guy Bartal and Mordechai Segev. Israel Science Foundation (ISF), 3620/24, Guy Bartal. Deutsche Forschungsgemeinschaft, SE 2153/3-1, Guy Bartal, Meir Orenstein and Mordechai Segev.

Data availability
The data supporting the findings of this study are available from the corresponding authors upon reasonable request.

Code availability
The codes used to process the data are available from the corresponding authors upon reasonable request.

Declarations

Ethics approval and consent to participate
This manuscript did not relate to any human or animal experiment.

Competing interests
The authors declare no competing interests.

Received: 20 September 2025 Revised: 19 January 2026 Accepted: 20 January 2026
Published online: 07 April 2026

References

1. M.S. Tame et al., Quantum plasmonics. Nat. Phys. **9**, 329–340 (2013)
2. J. Wang, F. Sciarrino, A. Laing, M.G. Thompson, Integrated photonic quantum technologies. Nat. Photonics **14**, 273–284 (2020)
3. A. Faraon et al., Coherent generation of non-classical light on a chip via photon-induced tunnelling and blockade. Nat. Phys. **4**, 859–863 (2008)
4. J.C. Loredo et al., Generation of non-classical light in a photon-number superposition. Nat. Photonics **13**, 803–808 (2019)
5. M. Erhard, R. Fickler, M. Krenn, A. Zeilinger, Twisted photons: new quantum perspectives in high dimensions. Light: Sci. Appl. **7**, 17146–17146 (2017)
6. I.B. Djordjevic, Multidimensional QKD Based on Combined Orbital and Spin Angular Momenta of Photon. IEEE Photonics J. **5**, 7600112–7600112 (2013)
7. C.H. Bennett, G. Brassard, Quantum cryptography: public key distribution and coin tossing. Theor. Comput. Sci. **560**, 7–11 (2014)
8. R. Renner, N. Gisin, B. Kraus, Information-theoretic security proof for quantum-key-distribution protocols. Phys. Rev. A **72**, 012332 (2005)
9. F. Marsili et al., Detecting single infrared photons with 93% system efficiency. Nat. Photonics **7**, 210–214 (2013)
10. D.V. Reddy, R.R. Nerem, S.W. Nam, R.P. Mirin, V.B. Verma, Superconducting nanowire single-photon detectors with 98% system detection efficiency at 1550nm. Optica **7**, 1649 (2020)
11. J.L. O'Brien, A. Furusawa, J. Vučković, Photonic quantum technologies. Nat. Photonics **3**, 687–695 (2009)
12. K. Alexander et al., A manufacturable platform for photonic quantum computing. Nature **641**, 876–883 (2025)
13. A. Crespi et al., Integrated photonic quantum gates for polarization qubits. Nat. Commun. **2**, 566 (2011)
14. L.S. Madsen et al., Quantum computational advantage with a programmable photonic processor. Nature **606**, 75–81 (2022)
15. E. Pelucchi et al., The potential and global outlook of integrated photonics for quantum technologies. Nat. Rev. Phys. **4**, 194–208 (2021)
16. M. Krenn, A. Hochrainer, M. Lahiri, A. Zeilinger, Entanglement by path identity. Phys. Rev. Lett. **118**, 080401 (2017)
17. M. Halder et al., Entangling independent photons by time measurement. Nat. Phys. **3**, 692–695 (2007)
18. C. Reimer et al., Generation of multiphoton entangled quantum states by means of integrated frequency combs. Science **351**, 1176–1180 (2016)
19. T. Stav et al., Quantum entanglement of the spin and orbital angular momentum of photons using metamaterials. Science **361**, 1101–1104 (2018)
20. A. Mair, A. Vaziri, G. Weihs, A. Zeilinger, Entanglement of the orbital angular momentum states of photons. Nature **412**, 313–316 (2001)
21. E. Nagali et al., Quantum information transfer from spin to orbital angular momentum of photons. Phys. Rev. Lett. **103**, 013601 (2009)
22. C. Wu et al., Room-temperature on-chip orbital angular momentum single-photon sources. Sci. Adv. (2022). https://doi.org/10.1126/sciadv.abk3075
23. Y. Shen et al., Optical vortices 30 years on: oam manipulation from topological charge to multiple singularities. Light Sci. Appl. **8**, 90 (2019)
24. M. Müller, S. Bounouar, K.D. Jöns, M. Glässl, P. Michler, On-demand generation of indistinguishable polarization-entangled photon pairs. Nat. Photonics **8**, 224–228 (2014)
25. C. Simon, J.-W. Pan, Polarization entanglement purification using spatial entanglement. Phys. Rev. Lett. **89**, 257901 (2002)
26. P.G. Kwiat et al., New High-Intensity Source of Polarization-Entangled Photon Pairs. Phys. Rev. Lett. **75**, 4337–4341 (1995)
27. L. Allen, M.W. Beijersbergen, R.J.C. Spreeuw, J.P. Woerdman, Orbital angular momentum of light and the transformation of Laguerre-Gaussian laser modes. Phys. Rev. A **45**, 8185–8189 (1992)
28. R.A. Beth, Mechanical detection and measurement of the angular momentum of light. Phys. Rev. **50**, 115–125 (1936)
29. R. Fickler et al., Quantum entanglement of high angular momenta. Science **338**, 640–643 (2012)
30. R. Fickler et al., Interface between path and orbital angular momentum entanglement for high-dimensional photonic quantum information. Nat. Commun. **5**, 4502 (2014)
31. J. Wang et al., Terabit free-space data transmission employing orbital angular momentum multiplexing. Nat. Photonics **6**, 488–496 (2012)
32. L.J. Kong et al., Manipulation of eight-dimensional Bell-like states. Sci. Adv. (2019). https://doi.org/10.1126/sciadv.aat9206
33. J. Ma et al., Bright single-photon skyrmion sources in bullseye cavities. Nanophotonics **14**, 4411–4418 (2025)
34. J. Ma et al., Nanophotonic quantum skyrmions enabled by semiconductor cavity quantum electrodynamics. Nat. Phys. **21**, 1462–1468 (2025)
35. P. Ornelas, I. Nape, R. de Mello Koch, A. Forbes, Topological rejection of noise by quantum skyrmions. Nat. Commun. **16**, 2934 (2025)
36. P. Ornelas, I. Nape, R. de Mello Koch, A. Forbes, Non-local skyrmions as topologically resilient quantum entangled states of light. Nat. Photonics **18**, 258–266 (2024)
37. R. de Mello Koch, B. Q. Lu, P. Ornelas, I. Nape, A. Forbes, Quantum skyrmions in general quantum channels. APL Quantum 2, (2025).
38. Y. Gorodetski, A. Niv, V. Kleiner, E. Hasman, Observation of the spin-based plasmonic effect in nanoscale structures. Phys. Rev. Lett. **101**, 043903 (2008)
39. K.Y. Bliokh, F.J. Rodríguez-Fortuño, F. Nori, A.V. Zayats, Spin–orbit interactions of light. Nat. Photonics **9**, 796–808 (2015)
40. S. Tsesses et al., Optical skyrmion lattice in evanescent electromagnetic fields. Science **361**, 993–996 (2018)
41. L. Du, A. Yang, A.V. Zayats, X. Yuan, Deep-subwavelength features of photonic skyrmions in a confined electromagnetic field with orbital angular momentum. Nat. Phys. **15**, 650–654 (2019)
42. C.-F. Li, Spin and orbital angular momentum of a class of nonparaxial light beams having a globally defined polarization. Phys. Rev. A **80**, 063814 (2009)
43. Y. Zhao, J.S. Edgar, G.D.M. Jeffries, D. McGloin, D.T. Chiu, Spin-to-orbital angular momentum conversion in a strongly focused optical beam. Phys. Rev. Lett. **99**, 073901 (2007)
44. P. Das, L.-P. Yang, Z. Jacob, What are the quantum commutation relations for the total angular momentum of light? Tutorial. J. Opt. Soc. Am. B Opt. Phys. **41**, 1764 (2024)
45. M. Krenn, N. Tischler, A. Zeilinger, On small beams with large topological charge. New J. Phys. **18**, 033012 (2016)
46. A. Kam et al., Near-field photon entanglement in total angular momentum. Nature **640**, 634–640 (2025)
47. Y. Shen et al., Optical skyrmions and other topological quasiparticles of light. Nat. Photonics **18**, 15–25 (2024)
48. S. Tsesses, K. Cohen, E. Ostrovsky, B. Gjonaj, G. Bartal, Spin-orbit interaction of light in plasmonic lattices. Nano Lett. **19**, 4010–4016 (2019)
49. S. Gao et al., Paraxial skyrmionic beams. Phys. Rev. A **102**, 053513 (2020)
50. W. Lin, Y. Ota, Y. Arakawa, S. Iwamoto, On-chip optical skyrmionic beam generators. Optica **11**, 1588 (2024)

51. Y. Shen, E.C. Martínez, C. Rosales-Guzmán, Generation of optical skyrmions with tunable topological textures. ACS Photonics **9**, 296–303 (2022)
52. S. Donati et al., Twist of generalized skyrmions and spin vortices in a polariton superfluid. Proc. Natl. Acad. Sci. U. S. A. **113**, 14926–14931 (2016)
53. A. Srinivasa Rao, Optical skyrmions in the Bessel profile. J. Opt. Soc. Am. A **41**, 1059 (2024)
54. Y. Shen, H. Wang, S. Fan, Free-space topological optical textures: tutorial. Adv. Opt. Photonics **17**, 295 (2025)
55. Y. Shen, Y. Hou, N. Papasimakis, N.I. Zheludev, Supertoroidal light pulses as electromagnetic skyrmions propagating in free space. Nat. Commun. **12**, 5891 (2021)
56. G. Spektor, A. David, B. Gjonaj, G. Bartal, M. Orenstein, Metafocusing by a metaspiral plasmonic lens. Nano Lett. **15**, 5739–5743 (2015)
57. A. David, B. Gjonaj, Y. Blau, S. Dolev, G. Bartal, Nanoscale shaping and focusing of visible light in planar metal–oxide–silicon waveguides. Optica **2**, 1045 (2015)
58. H. Kim et al., Synthesis and dynamic switching of surface plasmon vortices with plasmonic vortex lens. Nano Lett. **10**, 529–536 (2010)
59. J. Kher-Aldeen et al., Dynamic control and manipulation of near-fields using direct feedback. Light: Sci. Appl. **13**, 298 (2024)
60. F. Machado, N. Rivera, H. Buljan, M. Soljačić, I. Kaminer, Shaping polaritons to reshape selection rules. ACS Photonics **5**, 3064–3072 (2018)
61. D. Lopez-Mago, J.C. Gutiérrez-Vega, Shaping Bessel beams with a generalized differential operator approach. J. Opt. **18**, 095603 (2016)
62. W.C. Soares, D.P. Caetano, J.M. Hickmann, Hermite-bessel beams and the geometrical representation of nondiffracting beams with orbital angular momentum. Opt. Express **14**, 4577 (2006)
63. G. Milione, H.I. Sztul, D.A. Nolan, R.R. Alfano, Higher-Order Poincaré Sphere, Stokes Parameters, and the Angular Momentum of Light. Phys. Rev. Lett. **107**, 053601 (2011)
64. Y. Ilin, I. Arad, Learning a quantum channel from its steady-state. New J. Phys. **26**, 073003 (2024)
65. Y. Ilin, I. Arad, Dissipative variational quantum algorithms for Gibbs state preparation. IEEE Trans. Quantum Eng. **6**, 1–12 (2025)
66. A. Pesah et al., Absence of barren plateaus in Quantum Convolutional Neural Networks. Phys. Rev. X **11**, 041011 (2021)
67. M. Cramer et al., Efficient quantum state tomography. Nat. Commun. **1**, 149 (2010)
68. M. Christandl, R. Renner, Reliable quantum state tomography. Phys. Rev. Lett. **109**, 120403 (2012)
69. G. Torlai et al., Neural-network quantum state tomography. Nat. Phys. **14**, 447–450 (2018)
70. L. Rippe, B. Julsgaard, A. Walther, Y. Ying, S. Kröll, Experimental quantum-state tomography of a solid-state qubit. Phys. Rev. A **77**, 022307 (2008)
71. J.B. Altepeter, E.R. Jeffrey, P.G. Kwiat, Photonic state tomography. Adv. At. Mol. Opt. Phys. **52**, 105–159 (2005)
72. A.I. Lvovsky, M.G. Raymer, Continuous-variable optical quantum-state tomography. Rev. Mod. Phys. **81**, 299–332 (2009)
73. X. Lei, Q. Zhan, Topological quasiparticles of light: from spin-orbit coupling to photonic skyrmions. Laser Photon. Rev. (2025). https://doi.org/10.1002/lpor.202501427
74. J. Chen, A. Forbes, C.-W. Qiu, More than just a name? From magnetic to optical skyrmions and the topology of light. Light Sci. Appl. **14**, 28 (2025)
75. Z. Guo, C. Peters, N. Mata-Cervera et al., Topological robustness of classical and quantum optical skyrmions in atmospheric turbulence. Nat. Commun. (2026). https://doi.org/10.1038/s41467-026-68751-3
76. B.P. da Silva, D.S. Tasca, E.F. Galvão, A.Z. Khoury, Astigmatic tomography of orbital-angular-momentum superpositions. Phys. Rev. A **99**, 043820 (2019)
77. T. Bauer et al., Ultrafast time dynamics of plasmonic fractional orbital angular momentum. ACS Photonics **10**, 4252–4258 (2023)
78. L. Fridman, et al. Hyperentanglement in nanophotonic systems with discrete rotational symmetry. arXiv preprint arXiv:2511.00860 (2025).
79. L. Nemirovsky-Levy et al., Nonlinear nanophotonics for high-dimensional quantum states. Light Sci. Appl. **15**(1), 92 (2026)
80. M. Kauranen, A.V. Zayats, Nonlinear plasmonics. Nat. Photonics **6**, 737–748 (2012)
81. K. Frischwasser et al., Real-time sub-wavelength imaging of surface waves with nonlinear near-field optical microscopy. Nat. Photonics **15**, 442–448 (2021)
82. A. Karnieli et al., Emulating spin transport with nonlinear optics, from high-order skyrmions to the topological Hall effect. Nat. Commun. **12**(1), 1092 (2021)